metals

MDPI

Article

A Combined Hybrid 3-D/2-D Model for Flow and Solidification Prediction during Slab Continuous Casting

Mujun Long *, Huabiao Chen, Dengfu Chen *, Sheng Yu, Bin Liang and Huamei Duan

College of Materials Science and Engineering, Chongqing University, Chongqing 400044, China; chenhuabiao@cqu.edu.cn (H.C.); jscquys@163.com (S.Y.); binliang@cqu.edu.cn (B.L.); duanhuamei@cqu.edu.cn (H.D.)

* Correspondence: longmujun@cqu.edu.cn (M.L.); chendfu@cqu.edu.cn (D.C.); Tel.: +86-23-6510-2467 (M.L. & D.C.)

Received: 11 December 2017; Accepted: 8 March 2018; Published: 14 March 2018

Abstract: A combined hybrid 3-D/2-D simulation model was developed to investigate the flow and solidification phenomena in turbulent flow and laminar flow regions during slab continuous casting (CC). The 3-D coupling model and 2-D slicing model were applied to the turbulent flow and laminar flow regions, respectively. In the simulation model, the uneven distribution of cooling water in the width direction of the strand was taken into account according to the nozzle collocation of secondary cooling zones. The results from the 3-D turbulent flow region show that the impact effect of the molten steel jet on the formation of a solidification shell is significant. The impact point is 457 mm below the meniscus, and the plug flow is formed 2442 mm below the meniscus. In the laminar flow region, grid independence tests indicate that the grids with a cell size of 10×10 mm^2 are sufficient in simulations to attain the precise temperature distribution and solidification profile. The liquid core of the strand is not entirely uniform, and the solidification profile agrees well with the integrated distribution of cooling water in secondary cooling zones. The final solidification points are at a position of 400–500 mm in the width direction and are 17.66 m away from the meniscus.

Keywords: slab continuous casting; hybrid simulation model; uneven secondary cooling

1. Introduction

Continuous casting (CC) technology has become the primary method of producing steel strands in the steelmaking industry. During the CC process, the molten steel is continuously fed into the water-cooled mold through a submerged entry nozzle (SEN) and a solidified shell of sufficient thickness is formed. Subsequently, the strand is pulled into the secondary cooling zones and cooled by water spray or air-mist spray in order to solidify completely. The strand quality, particularly regarding surface and inner cracks, is closely related to the turbulent flow and the heat transfer during the solidification involved in a CC process [1–5]. This is particularly true given that, in the slab CC process, the solidification profile of the slab transverse section—which closely relates to the integrated distribution of cooling water in secondary cooling zones—is not entirely uniform [6–8]. This effect on centerline segregation is significant [7,9,10].

To date, both a two-dimensional (2-D) slicing model and three-dimensional (3-D) coupling model are widely used to predict the flow and solidification phenomena during the CC process. Owing to the high calculation efficiency, the 2-D slicing model is widely used to predict the temperature distribution and solidification profile during the CC process [7,10–12]. The calculation efficiency of the 2-D slicing model is improved by using an effective thermal conductivity concept to indirectly take the flow effect into account. However, the 2-D slicing model assumes that the solidification shell is a heat-transfer

slice which moves from the meniscus to the solidification end. Evidently, the effect of turbulent flow on temperature distribution and the solidification shell is not directly considered in the 2-D slicing model. In fact, especially for slab the CC process, the molten steel jet which impacts the narrow face has a significant effect on the temperature distribution and solidification shell [13]. Hence, to consider the effect of turbulent flow, the 3-D coupling model has been applied during the CC process [13–17]. Compared with the 2-D slicing model, the computational domain is much larger. Thereby, the amount of calculation is very large. Furthermore, the integrated distribution of cooling water in the width directions of secondary cooling zones is not considered in the previous 3-D calculations [13,17]. This simple treatment of the heat transfer condition would evidently affect the accurate prediction of the solidification profile. Recently, Sun et al. [18] proposed a method to divide the computational domain of the CC bloom to improve the calculation efficiency. However, in that simulation model, the grid independence tests were not carried out and the heat transfer coefficient was assumed to be constant around the strand transverse section. Moreover, compared with the bloom, the heat transfer boundary of the CC slab is more complex. In the width direction, the distribution of the cooling water is not entirely uniform. Thus far, the combined hybrid 3-D/2-D numerical model has not been used in the simulation of a slab CC process.

In the present work, to simultaneously consider the effect of turbulent flow and improve calculation efficiency, a combined hybrid 3-D/2-D numerical model was established and used to explore the transport phenomena during the slab CC process. The 3-D coupling model and 2-D slicing model were adopted in the turbulent flow region and laminar flow region, respectively. The effects of flow in the turbulent region on the temperature distribution and the location of the final solidification point are considered by the data of the interface in the 3-D turbulent flow region. These are transmitted to the 2-D slice as the initial conditions. The grid independence tests were carried out to find a suitable mesh cell size. This was then adopted in the simulation of the laminar flow region. In the present model, the distribution of cooling water in the width direction was taken into account.

2. Model Description

2.1. Mathematical Formulation

The continuity equation is

$$\frac{\partial \rho}{\partial t} + \frac{\partial (\rho u_i)}{\partial x_i} = 0 \tag{1}$$

The momentum equation is

$$\frac{\partial (\rho u_i)}{\partial t} + \frac{\partial (\rho u_i u_j)}{\partial x_j} = -\frac{\partial P}{\partial x_i} + \frac{\partial}{\partial x_i}\left[\mu_{\text{eff}}\left(\frac{\partial u_i}{\partial x_j} + \frac{\partial u_j}{\partial x_i}\right)\right] + \rho g_i + S_{i,\text{mom}} \tag{2}$$

$$\mu_{\text{eff}} = \mu + \mu_t = \mu + c_\mu \rho \frac{k^2}{\varepsilon} \tag{3}$$

and

$$S_{i,\text{mom}} = \frac{(1 - f_{\text{L}})^2}{(f_{\text{L}}^3 + 0.01)} A_{\text{mushy}} (u_i - v_{i,p}) \tag{4}$$

$$f_{\text{L}} = \begin{cases} 0 & T < T_{\text{Solidus}} \\ \frac{T - T_{\text{solidus}}}{T_{\text{Liquidus}} - T_{\text{Solidus}}} & T_{\text{Solidus}} < T < T_{\text{Liquidus}} \\ 1 & T > T_{\text{Liquidus}} \end{cases} \tag{5}$$

where ρ, t, u_i, u_j, μ_{eff}, P, g_i, f_{L}, A_{mushy}, $v_{i,p}$, T, T_{Solidus}, and T_{Liquidus} are molten steel density (kg/m^3), time (s), i-component of velocity (m/s), j-component of velocity (m/s), effective viscosity (kg·m^{-1}·s^{-1}), pressure (N/m^2), i-component of acceleration due to gravity (m/s^2), liquid fraction, morphology constant, i-component of casting speed (m/s), temperature (K), solidus temperature (K), and liquidus

temperature (K), respectively. The value of A_{mushy} is usually between 10^5 and 10^8 in the numerical modelling of CC processes. In addition, the higher the value of A_{mushy}, the steeper the transition of the velocity of the material to zero as it solidifies. Values between 10^4 and 10^7 are recommended for most computations (based on the user's guide of Ansys Fluent 14.0). Based on these two things, the value of A_{mushy} was set to 10^7 in the present work.

Standard k-ε equations are

$$\frac{\partial(\rho k)}{\partial t} + \frac{\partial(\rho k u_i)}{\partial x_i} = \frac{\partial}{\partial x_i}\left(\frac{\mu_t}{\sigma_k}\frac{\partial k}{\partial x_j}\right) + G - \rho\varepsilon + S_k \tag{6}$$

$$\frac{\partial(\rho \varepsilon)}{\partial t} + \frac{\partial(\rho \varepsilon u_i)}{\partial x_i} = \frac{\partial}{\partial x_i}\left(\frac{\mu_t}{\sigma_\varepsilon}\frac{\partial \varepsilon}{\partial x_j}\right) + c_1\frac{\varepsilon}{k}G - c_2\frac{\varepsilon^2}{k}\rho + S_\varepsilon \tag{7}$$

where

$$G = \mu_t \frac{\partial u_i}{\partial x_j}\left(\frac{\partial u_i}{\partial x_j} + \frac{\partial u_j}{\partial x_i}\right) \tag{8}$$

$$S_k = \frac{(1-f_{\text{L}})^2}{\left(f_{\text{L}}^3 + 0.01\right)} A_{\text{mushy}} k \tag{9}$$

$$S_\varepsilon = \frac{(1-f_{\text{L}})^2}{\left(f_{\text{L}}^3 + 0.01\right)} A_{\text{mushy}} \varepsilon \tag{10}$$

where G, k, ε, μ, and μ_t are the generation of turbulence kinetic energy ($\text{kg}\cdot\text{m}^{-1}\cdot\text{s}^{-3}$), turbulent kinetic energy (m^2/s^2), dissipation rate of turbulence energy (m^2/s^3), molecular viscosity ($\text{kg}\cdot\text{m}^{-1}\cdot\text{s}^{-1}$), and turbulent viscosity ($\text{kg}\cdot\text{m}^{-1}\cdot\text{s}^{-1}$), respectively. The standard values of σ_k, σ_ε, c_1, c_2, and c_μ recommended by Launder and Spalding are 1.0, 1.3, 1.44, 1.92, and 0.09, respectively.

The energy equation is

$$\frac{\partial(\rho H)}{\partial t} + \frac{\partial(\rho u_i H)}{\partial x_i} = \frac{\partial}{\partial x_i}\left[\left(\lambda + \frac{c_p \mu_t}{Pr_t}\right)\frac{\partial T}{\partial x_i}\right] \tag{11}$$

where

$$H = h + \Delta H = h_{\text{ref}} + \int_{T_{\text{ref}}}^{T} c_p \text{d}T + f_{\text{L}} L \tag{12}$$

where H, Pr_t, h, L, λ, and c_p, are enthalpy (J/kg), turbulent Prandtl number, sensible enthalpy (J/kg), pure solvent melting heat (J/kg), thermal conductivity ($\text{W}\cdot\text{m}^{-1}\cdot\text{K}^{-1}$), and specific heat ($\text{J}\cdot\text{kg}^{-1}\cdot\text{K}^{-1}$), respectively. The value of Pr_t was set to 0.85 (based on the theory guide of Ansys Fluent 14.0). More details about the mathematical formulation are available in reference [14].

2.2. Computational Domain

According to the geometric symmetry, the strand was assumed to be ideally symmetrical and a quarter of the strand was selected to be calculated. The geometry and working parameters of the CC process are listed in Table 1. The whole 3-D computational domain ($1530 \times 190 \times 20{,}362$ mm^3) is very large. If the coupled model is adopted in it directly, the cost of computation will be very large. To cut down the great amount of calculation and improve the calculation efficiency, the computational domain is suitably divided into two parts, the 3-D turbulence region and the 2-D laminar flow region. The division method is illustrated in Figure 1. When the z-component velocity of molten steel is equal to the casting speed, the plug flow is formed. This means that the local molten steel and shell are in a relatively static status. That is, the first transverse section of the strand—where z-component velocities equal to the casting speed—is the interface between the turbulent flow region and laminar

flow region. The data of the interface in the 3-D turbulent flow region are transmitted to the initial 2-D slice in the laminar flow region using a coordinate interpolation algorithm.

Table 1. The geometry and working parameters of the CC (continuous casting) process.

Parameters	Values	Secondary Cooling	Length (mm)	Cooling Water Flow Rate (L/min)
Mold section	1530 × 190 mm^2	Zone 1	405	155
Mold length	800 mm	Zone 2	555	84
Inside size of SEN	86 × 45 mm^2	Zone 3	800	54
Outside size of SEN	141 × 100 mm^2	Zone 4	1730	65
Port size of SEN	45 × 73 mm^2	Zone 5	1927	52
Port angle	−15 degrees	Zone 6	3854	86
Casting speed	1.2 m/min	Zone 7	5806	86
Casting temperature	1811 K	Zone 8	4485	59
Steel grade	Q345	-	-	-

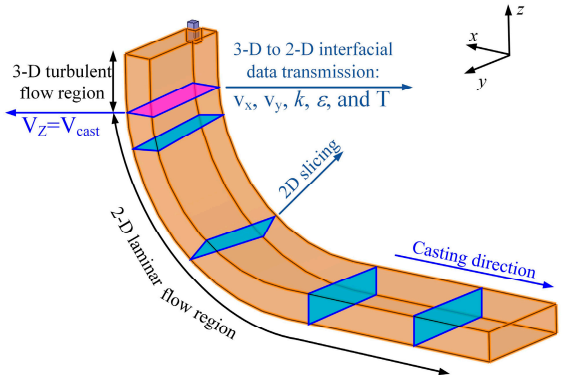

Figure 1. Illustration of 3-D turbulent flow and 2-D laminar flow regions during the CC (continuous casting) process.

In order to find out the interface between the 3-D turbulent flow region and the 2-D laminar region, a computational domain with a size of 1530 × 190 × 3250 mm^3 was built and calculated. The position of this interface can be obtained by analyzing the *z*-component velocity variation of molten steel at the central symmetry plane of strand narrow face. The meshes created by ANSYS ICEM CFD 14.0 and adopted in 3-D turbulent flow region and 2-D laminar flow region are shown in Figure 2. The number of elements for the meshes of the 3-D part and 2-D part are 517,793 and 770, respectively.

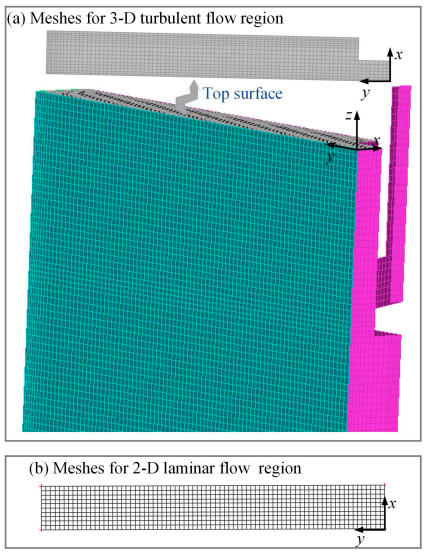

Figure 2. Meshes adopted in the (**a**) 3-D turbulent flow region and (**b**) 2-D laminar flow region.

2.3. Boundary Conditions and Physical Properties

The inlet velocity of SEN was calculated based on mass conservation. The k and ε values were estimated using the semi-empirical relations. The values of these parameters are v_{in} = 1.502 m/s, k = 0.003 m^2/s^2, ε = 0.0134 m^2/s^3, and T = 1811 K. The boundary condition of the outlet in the 3-D part was set as 'outflow'. The wall condition was employed on the meniscus without heat transfer.

The wall condition was employed on the strand surface. The heat flux of the mold surface was calculated using Equation (13) [19].

$$q_{\text{m}} = 2,680,000 - 276,000 \times \sqrt{\frac{60L_z}{v_c}} \tag{13}$$

where L_z and v_c are the distance from the meniscus (m) and the casting speed (m/min), respectively.

In the secondary cooling zone, the cooling types include four aspects: water spray cooling, radiation cooling, water evaporation cooling, and roll contact cooling. In the present work, four aspects of cooling types have been considered. First, we determined the heat conditions for different cooling types with the same method described in our publications [7,9]. The heat flux for the water spray cooling region was calculated using Equation (14). More detailed descriptions about the other three cooling types in the secondary cooling zone are available in our publications [7,9]. Then, to simplify this heat transfer process, we use the integrated heat transfer coefficient (in which the four cooling types have been taken into account) to describe the heat transfer process.

$$q_{\text{s}} = h(T_{\text{w}} - T_0) = \left(2950.190 \times T_{\text{w}}^{-0.235} \times w^{0.805}\right)(T_{\text{w}} - T_0) \tag{14}$$

where w, T_{w}, and T_0 are the spray water impingement density ($\text{L}\cdot\text{m}^{-2}\cdot\text{s}^{-1}$), slab surface, and water temperature, respectively.

Due to the existence of spray water overlap, the distribution of spray water for each row of nozzles along the width direction should be identified based on the nozzle collocation, as shown in Figure 3a. More details about this technique are available in our publication [7]. According to the nozzle collocation of secondary cooling zones, the integrated distribution of cooling water from Zone 1 to Zone 8 is obtained, as shown in Figure 3b. In order to deal with the heat transfer condition conveniently, the strand surface in the width direction is divided into 26 pieces (sections No. 1 to No. 25 being 30 mm wide and section No. 26 being 15 mm wide) for heat transfer. The cooling water sprayed onto each piece is determined based on the nozzle collocation of each cooling zone. The cooling water on each piece is supposed to be uniformly distributed.

The physical properties of steel Q345 used in the calculation are listed in Table 2.

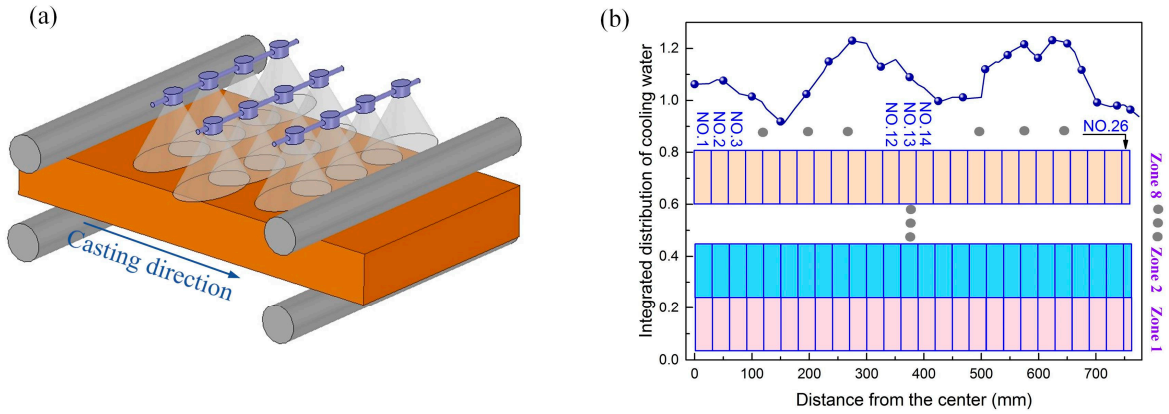

Figure 3. (**a**) Schematic of nozzle collocation; (**b**) integrated distribution of cooling water from Zone 1 to Zone 8.

Table 2. Physical properties of steel Q345.

Physical Properties	Values	Physical Properties	Values
Density, kg/m^3	7330	Viscosity, kg·(m·s)$^{-1}$	0.0062
Specific heat, J (kg·K)$^{-1}$	319.59 + 0.1934 × T (K)	Thermal conductivity, W (m·K)$^{-1}$	57.524 − 0.0164 × T (K)
Liquidus, K	1786	Solidus, K	1715
Latent heat, J/kg	255,500	-	-

2.4. Solution Procedure

The coupled calculation model was solved using the SIMPLE method with ANSYS Fluent 14.0. For both the 3-D turbulent flow region and the 2-D laminar flow region, the time step size was set to 0.05 s. Based on the relations between the length of model and casting speed, the total number of time steps for 3-D turbulent flow region and 2-D laminar flow region were 3500 and 17,802, respectively. The calculation was performed on a computer with a 3.50-GHz Intel Core i7-3770k processor and 16.0-GB RAM. For each time step, the tolerances of continuity, x-velocity, y-velocity, z-velocity, k, ε, and energy were set as 0.001, 0.001, 0.001, 0.001, 0.001, 0.001, and 1×10^{-6}, respectively.

3. Results and Discussion

3.1. Flow and Solidification Phenomena in the Turbulent Flow Region

Figure 4a shows the melt flow pattern in the turbulent flow region. It is seen that the molten steel jet flows through the port of SEN and impacts on the narrow face of the mold. The molten steel jet is divided into two parts at the impact point and forms upper and lower recirculation vortexes. The fresh molten steel with higher temperature is brought to the impact point, where the solidification shell is remelting. The remelting phenomenon of the solidification shell is shown in Figure 4b. It is obvious that the impact effect of the molten steel jet on the formation of the solidification shell near the impact point is remarkable.

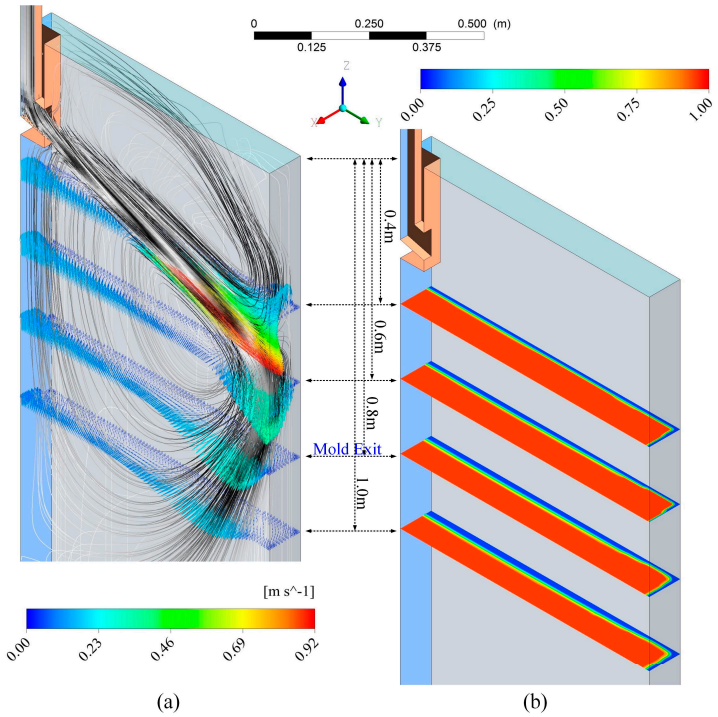

Figure 4. (**a**) Flow field in the turbulent flow region; (**b**) liquid fraction on the different transverse sections.

The impact point of the jet on the narrow face is obtained from Figure 5a,b. At the impact point, the *z*-component of velocity is equal to zero and the velocity magnitude reaches a valley value. In the present case, the impact point is at the position 457 mm below the meniscus. In order to find the interface between the turbulent flow region and the laminar flow region, the *z*-component of velocities of characteristic lines at the central symmetry plane of the strand narrow face were investigated. From Figure 5c, it can be seen that the *z*-component of the molten steel velocity is equal to the casting speed when arriving at the location 2442 mm below the meniscus, where it is roughly placed at the end of secondary cooling Zone 3.

To deal with the heat transfer condition for each secondary cooling zone separately, the transverse section at the end of secondary cooling Zone 3 (2560 mm below meniscus) is selected as the interface between the turbulent flow region and laminar flow region. Therefore, the 2-D slicing model is adopted in the laminar flow region from Zone 4 to Zone 8.

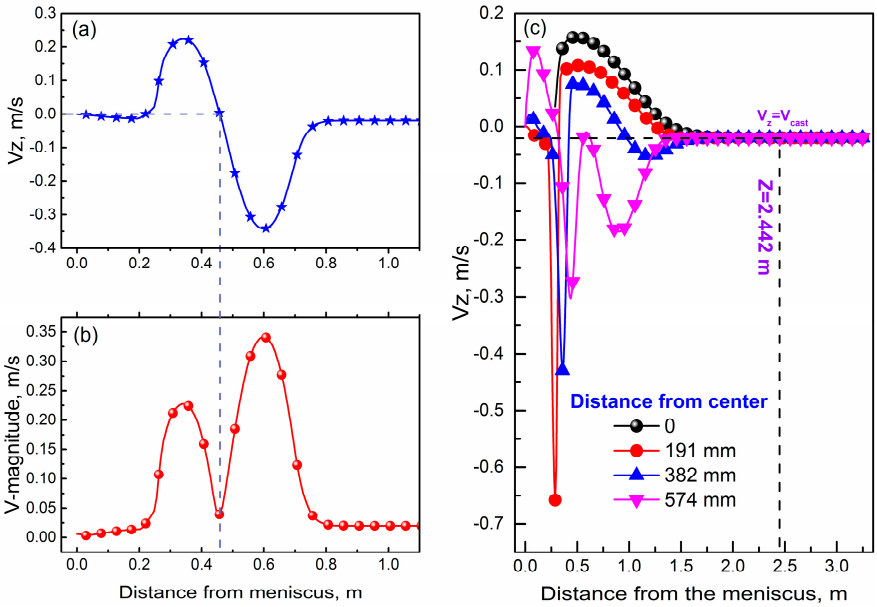

Figure 5. (**a**) *z*-component of velocity and (**b**) velocity magnitude variation of the line with 10 mm from the narrow face at the central symmetry plane. (**c**) *z*-component of the velocity variation of different lines at the central symmetry plane of the strand narrow face.

3.2. Grid Independence Tests for the Laminar Flow Region

To begin with, grid sizes for the laminar flow region have been carefully chosen to ensure the grid independence solution. As seen in the results of the grid independence tests shown in Figure 6, relatively larger differences exist in the solidification profile and temperature extreme in the transverse section (17.56 m from the meniscus) with different cell sizes. It is obvious that the cell size 25 × 25 mm^2, as shown in Figure 6a, is too large for this case to precisely predict the solidification profile and temperature distribution. The solidification profile does not correspond with the integrated distribution of cooling water in secondary cooling zones (shown in Figure 3). Also, the lowest temperature is higher than the other cases. In comparing Figure 6b,c, where the cell size decreases from 15 × 15 mm^2 to 10 × 10 mm^2, there is a similar solidification profile which is corresponding with the integrated distribution of cooling water in the width direction of strand. The maximum and minimum temperatures in the case where the cell size is 15 × 15 mm^2 are very close to those in the case where the cell size is 10 × 10 mm^2. When the cell size reduces from 10 × 10 mm^2 to 5 × 5 mm^2, as shown in Figure 6d, the temperature extreme of 1181 K to 1733 K shows little change compared with that using grids with a cell size of 10 × 10 mm^2. Thereby, in the present simulation, the grids with cell size 10 × 10 mm^2 are sufficient to obtain the precise temperature distribution and solidification profile.

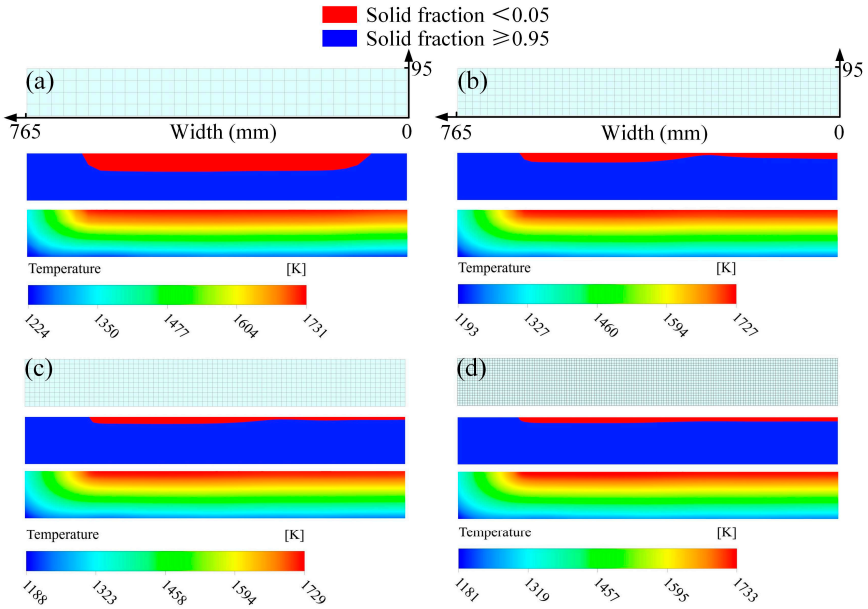

Figure 6. Solidification profile and temperature field in the transverse section (17.56 m from the meniscus) with different cell sizes: (**a**) 25 × 25 mm^2, (**b**) 15 × 15 mm^2, (**c**) 10 × 10 mm^2, (**d**) 5 × 5 mm^2.

3.3. Temperature Field and Solidification Profile

The slab center and wide surface center temperature along the casting direction predicted by the present model are compared to that predicted by our previous model, which is proven and widely employed in temperature prediction during the CC process. As the results show in Figure 7, the temperature predicted by the present model agrees well with that of the models by Long et al. [7] and Long and Chen [9]. The slab center temperature, as shown in Figure 7a, decreases slowly before complete solidification. However, after complete solidification, the slab center temperature decreases sharply. This is because there is no latent heat to maintain the temperature when the local region solidifies completely. The wide surface center temperature is shown in Figure 7b. Due to the strong cooling of the mold, the surface temperature decreases radically, and then recalesces when the strand is pulled out of the mold. In the secondary cooling zone, the surface temperature decreases gradually.

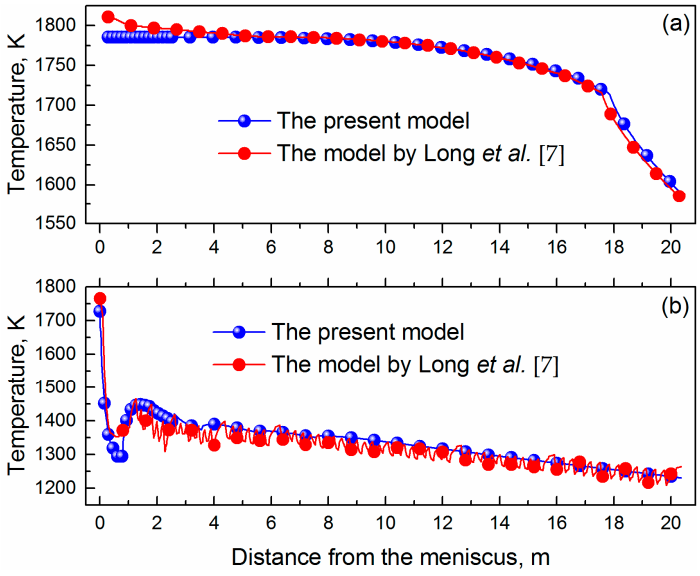

Figure 7. (**a**) Slab center and (**b**) wide surface center temperature along the casting direction.

The temperature distribution in transverse sections with different distances from the meniscus (as shown in Figure 8a) have a similar profile. The temperature decreases as the distance from the meniscus increases. Figure 8b shows the solidification profile evolution process during continuous casting. It is obvious that the liquid core of the strand is not entirely uniform. At the local region of the strand in the width direction, from roughly 400 to 500 mm, the molten steel solidifies completely owing to the minimum amount of the cooling water sprayed on it in the secondary cooling zone. The final solidification points (another one in the other half of the geometry) are 17.66 m away from the meniscus. Moreover, at the position about 150 mm in width direction, the molten steel solidifies completely a little earlier than that at the region from 400 to 500 mm. The reason is that the amount of cooling water at the former position is a little more than that at the region from 400 to 500 mm. This results from the valley of the distribution curve being very narrow at the position of about 150 mm, although the proportion of cooling water is slightly lower than that at the region from 400 to 500 mm. The solidification profile agrees well with the integrated distribution of cooling water in the secondary cooling zones.

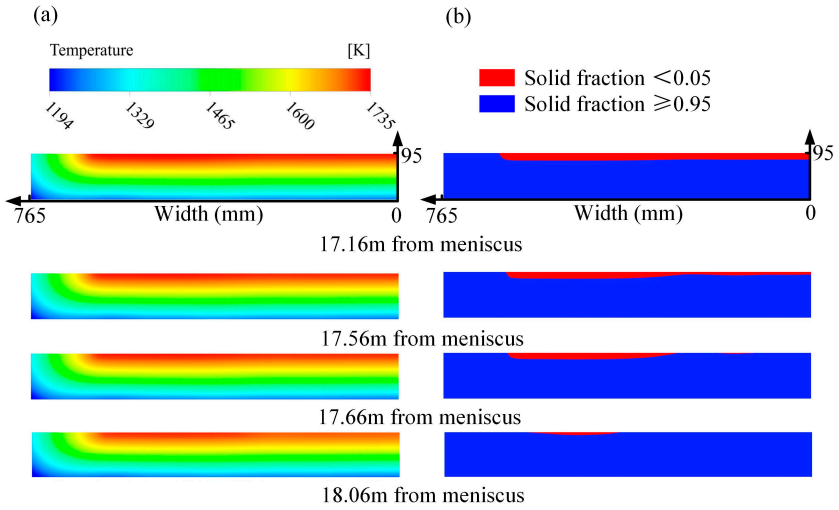

Figure 8. (**a**) Temperature field and (**b**) solidification profile in transverse sections with different distances from the meniscus.

4. Conclusions

A combined hybrid 3-D/2-D simulation model with a high calculation efficiency has been developed to investigate the flow and solidification behaviors during the slab CC process. The main conclusions are summarized as follows:

(1) The impact effect caused by the molten steel jet on the formation of a solidification shell is significant. The impact point is at the position 457 mm below the meniscus, and the plug flow is formed 2442 mm below the meniscus.

(2) For the simulation of the laminar flow region, the grids with a cell size of 10 × 10 mm^2 are sufficient to attain a precise temperature distribution and solidification profile.

(3) The solidification profile of the strand is not entirely uniform. The final solidification points, roughly being at the position from 400–500 mm in the width direction, are 17.66 m away from the meniscus.

Acknowledgments: The authors would like to thank the Natural Science Foundation of China (NSFC) for financial support (project No. 51504048, 51374260, 51611130062).

Author Contributions: Huabiao Chen, Mujun Long, and Dengfu Chen conceived the simulation model and the validation method. Huabiao Chen, Sheng Yu, Bin Liang, and Huamei Duan performed the calculations. All of the authors analyzed and discussed the data. Huabiao Chen wrote the paper.

Conflicts of Interest: The authors declare no conflict interest.

References

1. Ma, J.C.; Xie, Z.; Ci, Y.; Jia, G.L. Simulation and application of dynamic heat transfer model for improvement of continuous casting process. *Mater. Sci. Technol.* **2009**, *25*, 636–639. [CrossRef]
2. Zhao, Y.; Chen, D.F.; Long, M.J.; Shen, J.L.; Qin, R.S. Two-dimensional heat transfer model for secondary cooling of continuously cast beam blanks. *Ironmak. Steelmak.* **2014**, *41*, 377–386. [CrossRef]
3. Ma, J.C.; Lu, C.S.; Yan, Y.T.; Chen, L.Y. Design and application of dynamic secondary cooling control based on real time heat transfer model for continuous casting. *Int. J. Cast Met. Res.* **2014**, *27*, 135–140. [CrossRef]
4. He, D.F.; Chang, S.; Wang, H.B. Controlling transverse cracks of slab based on edge control technology. *J. Iron Steel Res. Int.* **2015**, *22*, 42–47. [CrossRef]
5. Chen, S.D.; Hu, Z.F.; Yuan, Y.Y.; Luo, Y.Z. Study on intermediate crack in continuous casting slab of medium carbon steel. *J. Iron Steel Res. Int.* **2011**, *18*, 383–388.
6. Long, M.J.; Chen, D.F.; Wang, Q.X.; Luo, D.H.; Han, Z.W.; Liu, Q.; Gao, W.X. Determination of CC slab solidification using nail shooting technique. *Ironmak. Steelmak.* **2012**, *39*, 370–377. [CrossRef]
7. Long, M.J.; Dong, Z.H.; Chen, D.F.; Liao, Q.; Ma, Y.G. Effect of uneven solidification on the quality of continuous casting slab. *Int. J. Mater. Prod. Technol.* **2013**, *47*, 216–232. [CrossRef]
8. Shen, H.F.; Hardin, R.A.; MacKenzie, R.; Beckermann, C. Simulation using realistic spray cooling for the continuous casting of multi-component steel. *J. Mater. Sci. Technol.* **2002**, *18*, 311–314.
9. Long, M.J.; Chen, D.F. Study on mitigating center macro-segregation during steel continuous casting process. *Steel Res. Int.* **2011**, *82*, 847–856. [CrossRef]
10. Ji, C.; Luo, S.; Zhu, M.; Sahai, Y. Uneven solidification during wide-thick slab continuous casting process and its influence on soft reduction zone. *ISIJ Int.* **2014**, *54*, 103–111. [CrossRef]
11. Xie, X.; Chen, D.F.; Long, H.J.; Long, M.J.; Lv, K. Mathematical modeling of heat transfer in mold copper coupled with cooling water during the slab continuous casting process. *Metall. Mater. Trans. B* **2014**, *45*, 2442–2452. [CrossRef]
12. Hardin, R.A.; Liu, K.; Kapoor, A.; Beckermann, C. A transient simulation and dynamic spray cooling control model for continuous steel casting. *Metall. Mater. Transf. B* **2003**, *34*, 297–306. [CrossRef]
13. Wang, Q.Q.; Zhang, L.F. Influence of FC-mold on the full solidification of continuous casting slab. *JOM* **2016**, *68*, 2170–2179. [CrossRef]
14. Shamsi, M.R.R.I.; Ajmani, S.K. Three dimensional turbulent fluid flow and heat transfer mathematical model for the analysis of a continuous slab caster. *ISIJ Int.* **2007**, *47*, 433–442. [CrossRef]
15. Shamsi, M.R.R.I.; Ajmani, S.K. Analysis of mould, spray and radiation zones of continuous billet caster by three-dimensional mathematical model based on a turbulent fluid flow. *Steel Res. Int.* **2010**, *81*, 132–141. [CrossRef]
16. Yang, J.W.; Du, Y.P.; Shi, R.; Cui, X.C. Fluid flow and solidification simulation in beam blank continuous casting process with 3d coupled model. *Iron Steel Res. Int.* **2006**, *13*, 17–21. [CrossRef]
17. Seyedein, S.H.; Hasan, M. A three-dimensional simulation of coupled turbulent flow and macroscopic solidification heat transfer for continuous slab casters. *Int. J. Heat Mass Transf.* **1997**, *40*, 4405–4423. [CrossRef]
18. Sun, H.B.; Zhang, J.Q. Study on the macrosegregation behavior for the bloom continuous casting: Model development and validation. *Metall. Mater. Transf. B* **2014**, *45*, 1133–1149. [CrossRef]
19. Cai, K.K. *Continuous Casting Mold*; Metallurgical Industry Press: Beijing, China, 2008; p. 6, ISBN 978-7-5024-4635-2.